*Progress In Electromagnetics Research C, Vol. 84, 87–101, 2018*

# Torque Ripple Suppression Control of Bearingless Brushless DC Motor in Wide Speed Regulation Range

**Yukun Sun, Kuan Zhang, Ye Yuan*, and Fan Yang**

**Abstract**—Bearingless brushless DC (BBLDC) motor in the flywheel energy storage system has advantages of low energy consumption, high critical speed and better speed adjustment performance. However, torque ripple exists inevitably due to the current commutation of the BBLDC motor and the wide range of speed changes when the flywheel energy storage system charges and discharges. In this frame, an approach of combining the direct torque control (DTC) with the current prediction control (CPC) is proposed to suppress torque ripple in wide speed regulation range. In this paper, the mathematical model of the BBLDC motor is given, and the principle of DTC scheme is introduced. On the basis of analyzing the causes of commutation torque ripple when using DTC scheme, CPC scheme is employed to minimize the commutation torque ripple by controlling the changes of phase current during commutation. During the non-commutation, the DTC is selected, and the CPC is selected during the commutation. Results show that the proposed approach is feasible, and torque ripple is effectively suppressed both in high speed and low speed. Moreover, this method has no effect on the suspension performance.

## 1. INTRODUCTION

Energy is essential in our lives, flywheel energy storage system (FESS) as a new type of energy storage device has become a hot topic for scholars. As one of the core parts of FES, the drive motor becomes the focus of research. Bearingless brushless DC (BBLDC) motor combines the advantages of the BLDC motor and magnetic bearing motor [1]. It is introduced for FESS drive motor with low energy consumption, high critical speed and good speed adjustment performance [2]. However, large torque ripple exists in the BBLDC motor due to cogging effect, non-ideal trapezoidal back electromotive force and current commutation, which affects its performance.

In order to reduce the torque ripples, DTC [3, 4], adaptive control [5], hysteresis current control, hybrid PWM chopper based overlapping and observers [6–8] have been proposed. Among these methods, DTC not only controls the torque directly but also has the advantages of simple structure, fast torque response and good robustness. In [9], a look-up table made up by rotor flux vector position and torque error for determining the space voltage vector is presented. In [10–12], flux linkage observation is omitted, and the results show that DTC without flux linkage observation is more effective for reducing torque ripples, thus easier to use for a fast, accurate and stable operation without complicated coordinate transformation. However, the commutation current cannot be immediately turned off and on, and the commutation torque ripple still exists at high speed. In this frame, an improvement torque controller is proposed [13] to calculate the applied voltage for each instantaneous torque. Commutation torque ripple can be reduced, but the back EMF waveform is assumed to be known a priori. In [14], space-vector modulation and DTC are combined to reduce torque and speed ripple, and inverter-switching frequency is fixed. However, the parameters of PI controller are difficult to set, and the fixed PI

*Received 21 March 2018, Accepted 4 May 2018, Scheduled 18 May 2018*
* Corresponding author: Ye Yuan (1000050003@ujs.edu.cn).
The authors are with the School of Electrical and Information Engineering, Jiangsu University, Zhenjiang 212013, China.

coefficients are sensitive to the parameters, speed and load of the motor, resulting in poor robustness. In [15], an approach of hybrid two- and three-phase conduction mode is employed. Results show that the commutation ripple has been reduced, but there are still distinct ripples in the current waveform, caused by the PWM control.

Current prediction control (CPC) has the advantages of high control precision, good controllability and easy realization. This algorithm predicts the future output response based on the known information, so actual output can follow the predicted trajectory. In [15], CPC is applied to the induction machine with a better current control performance. Reference [16] used CPC to reduce the commutation torque ripple of BLDC motor, keeping the non-commutation phase current constant as the control target. In [17], a method combines CPC with the PWM-ON is proposed, which modified the PWM-ON control method.

For the purpose of simultaneously achieving the suppression of the torque ripple at low speed and high speed in FESS, this paper proposes an approach combines CPC with DTC based on the approach presented in [10]. Firstly, the mathematical model of BBLDC motors and DTC principle is given, then the reason for generating commutation torque ripple when using DTC is explained. In order to minimize the torque ripple, during the non-commutation, the DTC is selected, and the CPC is selected during the commutation. This method not only has the advantage of the DTC, but also minimizes the torque ripple effectively at all ranges of speed. Finally, the effectiveness of the proposed method is validated by simulink.

## 2. MATHEMATICAL MODEL OF BEARINGLESS BRUSHLESS DC MOTOR

BBLDC motor is based on the traditional BLDC motor embedded in a set of suspension force windings in the stator slot. Normally the study of magnetic bearing motors is generally divided into motor torque subsystem and suspension subsystem. Through the control of torque winding and suspension winding, the stable running of the motor is realized.

### 2.1. Mathematical Model of Torque

The voltage equation of the BBLDC motor can be described by the following equations:

$$\begin{pmatrix} u_A \\ u_B \\ u_C \end{pmatrix} = \begin{pmatrix} R_s & 0 & 0 \\ 0 & R_s & 0 \\ 0 & 0 & R_s \end{pmatrix} \cdot \begin{pmatrix} i_a \\ i_b \\ i_c \end{pmatrix} + \begin{pmatrix} L-M & 0 & 0 \\ 0 & L-M & 0 \\ 0 & 0 & L-M \end{pmatrix} \cdot \begin{pmatrix} \dfrac{di_a}{dt} \\ \dfrac{di_b}{dt} \\ \dfrac{di_c}{dt} \end{pmatrix} + \begin{pmatrix} e_a \\ e_b \\ e_c \end{pmatrix} \quad (1)$$

where $u$, $i$ and $e$ denote the phase voltage, phase current and back EMF in phases $A$, $B$ and $C$, respectively.

Most of the power absorbed by the motor from the power source is converted into kinetic energy in addition to copper and iron. Neglecting mechanical and other losses, the electromagnetic torque can be expressed as:

$$T_e = \frac{e_a i_a + e_b i_b + e_c i_c}{\omega} \quad (2)$$

The equation of motion can be written as:

$$T_e = T_l + B\omega + J\frac{d\omega}{dt} \quad (3)$$

$T_e$ is the electromagnetic torque, $T_l$ the load torque, $B$ the friction coefficient, $J$ the inertia coefficient, and $\omega$ the angular velocity of rotor.

### 2.2. Mathematical Model of Suspension Force

Figure 1 shows a structure of BBLDC motor. It is a 12-slot and 4-pole BBLDC motor. $A$, $B$ and $C$ are motor windings to generate the electromagnetic torque, and the distribution and principle of

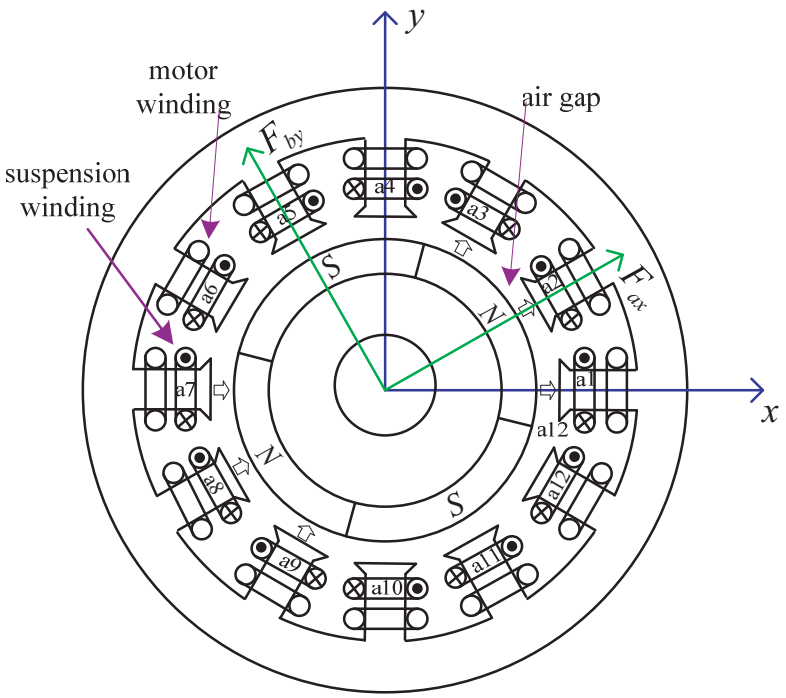


**Figure 1.** Structure of BBLDC motor.

electromagnetic torque generation are similar to the traditional BLDC motor. Windings a1 to a12 are suspension force windings which are additionally wound on the stator teeth to generate suspension force.

The principle of the suspension force generation is shown in Figure 1. When rotor angular position ranges from $-30°$ to $0°$, the currents in the suspension force windings as shown in the figure, torque windings and suspension force windings on the same stator do not conduct at the same time. The current values in windings a1, a2 and a3 are the same as in windings a7, a8 and a9, but in the opposite direction. The current values in windings a4, a5 and a6 are the same as in windings a10, a11 and a12, but in the opposite direction. The suspension force winding flux and permanent magnet field flux are superimposed each other. As a result, the magnetic balance in the air gap is broken, and electromagnetic forces $F_{ax}$ and $F_{by}$ are generated. By changing the magnitude and direction of the suspension force winding current, the suspension force in any direction in the *xoy* plane can be obtained. The phase of suspension force generation is shown in Figure 2.

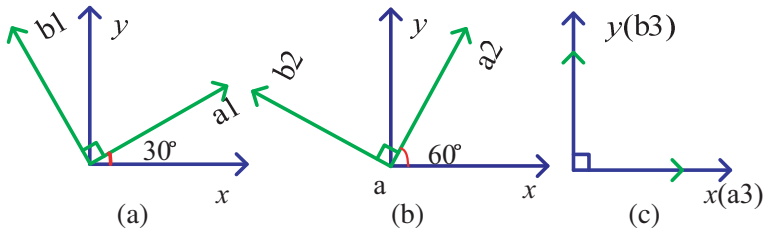


**Figure 2.** Phase of suspension force generation. (a) a1-b1. (b) a2-b2. (c) a3-b3.

When the rotor angular position ranges from $-30°$ to $0°$, $60°$ to $90°$, $150°$ to $180°$ and $240°$ to $270°$ suspension force is controlled by a1-b1 coordinate system defined in Figure 2(a). It can be expressed as:

$$\begin{pmatrix} F_{ax1} \\ F_{by1} \end{pmatrix} = \begin{pmatrix} K_i i_{ax1} + K_x x_1 \\ K_i i_{by1} + K_x y_1 \end{pmatrix} = K_i \begin{pmatrix} i_{ax1} \\ i_{by1} \end{pmatrix} + K_x \begin{pmatrix} x_1 \\ y_1 \end{pmatrix} \tag{4}$$

where $i_{ax1}$, $i_{bx1}$ are the suspension force winding currents; $x_1$, $y_1$ are the displacements along the a1-axis and b1-axis; $F_{ax1}$, $F_{by1}$ are the suspension forces along the a1-axis and b1-axis; $K_i$ is the current stiffness coefficient; $K_x$ is the displacement stiffness coefficient. Then the equation is transformed into the $xoy$ coordinate system.

$$\begin{aligned}\begin{pmatrix} F_x \\ F_y \end{pmatrix} &= \begin{pmatrix} \cos 30^\circ & \cos 120^\circ \\ \sin 30^\circ & \sin 120^\circ \end{pmatrix} \begin{pmatrix} F_{ax1} \\ F_{by1} \end{pmatrix} \\ &= K_i \begin{pmatrix} \cos 30^\circ & \cos 120^\circ \\ \sin 30^\circ & \sin 120^\circ \end{pmatrix} \begin{pmatrix} i_{ax1} \\ i_{by1} \end{pmatrix} + K_x \begin{pmatrix} \cos 30^\circ & \cos 120^\circ \\ \sin 30^\circ & \sin 120^\circ \end{pmatrix} \begin{pmatrix} x_1 \\ y_1 \end{pmatrix} \end{aligned} \tag{5}$$

where $F_x$, $F_y$ are the suspension forces along the $x$-axis and $y$-axis.

When the rotor angular position ranges from 0° to 30°, 90° to 120° 180° to 210° and 270° to 300° suspension force is controlled by the a2-b2 coordinate system defined in Figure 2(b).

$$\begin{pmatrix} F_{ax2} \\ F_{by2} \end{pmatrix} = \begin{pmatrix} K_i i_{ax2} + K_x x_2 \\ K_i i_{by2} + K_x y_2 \end{pmatrix} = K_i \begin{pmatrix} i_{ax2} \\ i_{by2} \end{pmatrix} + K_x \begin{pmatrix} x_2 \\ y_2 \end{pmatrix} \tag{6}$$

Then, the equation is transformed into the $xoy$ coordinate system.

$$\begin{aligned}\begin{pmatrix} F_x \\ F_y \end{pmatrix} &= \begin{pmatrix} \cos 60^\circ & \cos 150^\circ \\ \sin 60^\circ & \sin 150^\circ \end{pmatrix} \begin{pmatrix} F_{ax2} \\ F_{by2} \end{pmatrix} \\ &= K_i \begin{pmatrix} \cos 60^\circ & \cos 150^\circ \\ \sin 60^\circ & \sin 150^\circ \end{pmatrix} \begin{pmatrix} i_{ax2} \\ i_{by2} \end{pmatrix} + K_x \begin{pmatrix} \cos 60^\circ & \cos 150^\circ \\ \sin 60^\circ & \sin 150^\circ \end{pmatrix} \begin{pmatrix} x_2 \\ y_2 \end{pmatrix} \end{aligned} \tag{7}$$

When the rotor angular position ranges from 30° to 60°, 120° to 150°, 210° to 240° and 300° to 330° suspension force is controlled by the a3-b3 coordinate system defined in Figure 2(c).

$$\begin{pmatrix} F_{ax3} \\ F_{by3} \end{pmatrix} = \begin{pmatrix} K_i i_{ax3} + K_x x_3 \\ K_i i_{by3} + K_x y_3 \end{pmatrix} = K_i \begin{pmatrix} i_{ax3} \\ i_{by3} \end{pmatrix} + K_x \begin{pmatrix} x_3 \\ y_3 \end{pmatrix} \tag{8}$$

Then, the equation is transformed into the $xoy$ coordinate system.

$$\begin{pmatrix} F_x \\ F_y \end{pmatrix} = \begin{pmatrix} F_{ax3} \\ F_{by3} \end{pmatrix} = K_i \begin{pmatrix} i_{ax3} \\ i_{by3} \end{pmatrix} + K_x \begin{pmatrix} x_3 \\ y_3 \end{pmatrix} \tag{9}$$

## 3. DTC PLUS CPC CONTROL STRATEGY

### 3.1. Principle of DTC Scheme

#### *3.1.1. Voltage Space Vector*

BBLDC motor normally adopts two-phase conduction mode, so we can use a 6-digit to represent the switch status of the inverter, the 1 standards for connect while 0 standards for disconnect. Therefore, there are six connected stats for six different non-zero voltage space vectors: $v_1$ (100001), $v_2$ (001001), $v_3$ (011000), $v_4$ (010010), $v_5$ (000110) and $v_6$ (100100), as well as one zero voltage vector: $v_0$ (000000). Inverter state of different voltage vector space is shown in Figure 3(a).

Assuming that phase $A$ and phase $C$ are connected, the voltage space vector synthesized by conduction phase can be expressed as below:

$$v_1 = \frac{2}{3}\left(u_A + \alpha^2 u_C\right) = \frac{1}{\sqrt{3}} u_{dc} e^{j\frac{\pi}{6}}, \quad \alpha = e^{j\frac{2\pi}{3}} \tag{10}$$

Similarly, vectors for other five voltage space vectors are as indicated in formula (11).

$$\begin{cases} v_2 = \dfrac{2}{3}\left(\alpha u_B + \alpha^2 u_C\right) = \dfrac{1}{\sqrt{3}} u_{dc} e^{j\frac{\pi}{2}}, & v_3 = \dfrac{2}{3}\left(u_A + \alpha u_B\right) = \dfrac{1}{\sqrt{3}} u_{dc} e^{j\frac{5\pi}{6}} \\ v_4 = \dfrac{2}{3}\left(u_A + \alpha^2 u_C\right) = \dfrac{1}{\sqrt{3}} u_{dc} e^{j\frac{7\pi}{6}} & v_5 = \dfrac{2}{3}\left(\alpha u_B + \alpha^2 u_C\right) = \dfrac{1}{\sqrt{3}} u_{dc} e^{j\frac{3\pi}{2}} \\ v_6 = \dfrac{2}{3}\left(u_A + \alpha u_B\right) = \dfrac{1}{\sqrt{3}} u_{dc} e^{j\frac{11\pi}{6}} \end{cases} \tag{11}$$

The conduction phase voltage space vector distribution is shown in Figure 3(b). The conduction phase voltage vector acts as the boundary, and the space voltage vector plane is divided into six sectors.

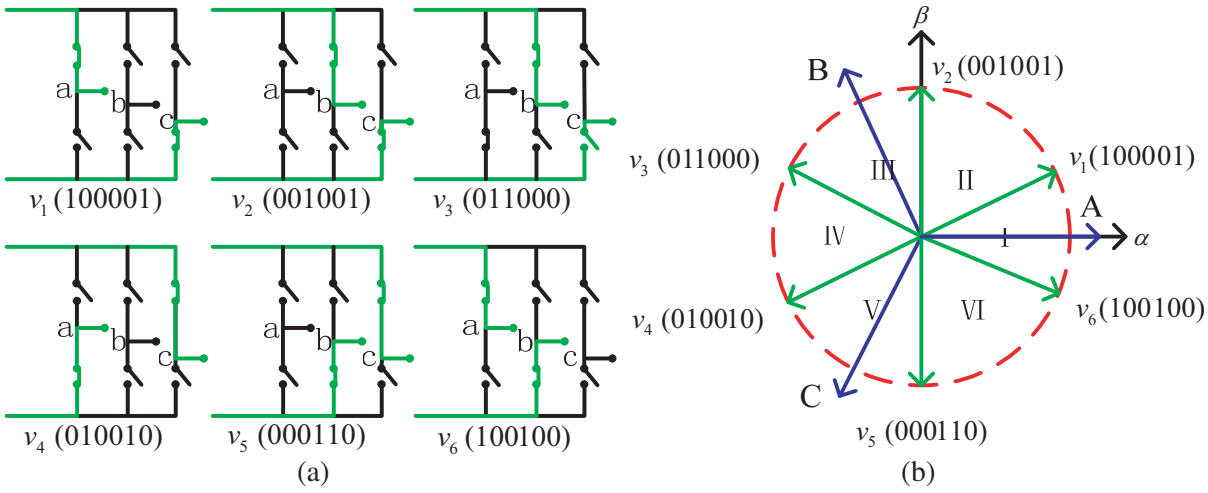


**Figure 3.** Inverter state and distribution of the voltage space vector. (a) Inverter state of different voltage space vector. (b) Distribution of the voltage space vector.

### *3.1.2. Electromagnetic Torque Estimation*

Electromagnetic torque estimation is an essential part of direct torque control, and Equation (2) is used to calculate the torque. In the actual control system, the back EMF of motor cannot be measured directly, but the phase-to-ground voltage, stator current and neutral-point voltage (for motors without neutral point, the neutral point can be modeled by a three-phase Y symmetric load in parallel on the stator) can be measured. Suppose that $Ux$ is the phase voltage, $ux$ the phase-to-ground voltage and $UN$ the neutral-point voltage, we can get the following equation.

$$ux = Ux + UN \quad (x \text{ represents } a,\ b \text{ and } c) \tag{12}$$

Substituting Equation (12) into Equation (1) yields:

$$\begin{pmatrix} e_a \\ e_b \\ e_c \end{pmatrix} = \begin{pmatrix} u_a - U_n \\ u_b - U_n \\ u_c - U_n \end{pmatrix} - \begin{pmatrix} R_s & 0 & 0 \\ 0 & R_s & 0 \\ 0 & 0 & R_s \end{pmatrix} \cdot \begin{pmatrix} i_a \\ i_b \\ i_c \end{pmatrix} - \begin{pmatrix} L-M & 0 & 0 \\ 0 & L-M & 0 \\ 0 & 0 & L-M \end{pmatrix} \cdot \begin{pmatrix} \dfrac{di_a}{dt} \\ \dfrac{di_b}{dt} \\ \dfrac{di_c}{dt} \end{pmatrix} \tag{13}$$

Therefore, according to Equation (13), the torque can be calculated.

### *3.1.3. Torque Control*

DTC selects the voltage space vector to control the speed of the stator flux, and then changes the flux angle, so as to achieve the purpose of control torque. BBLDC motor has position sensors, and the voltage space vector selected by position sensors can produce a hexagonal flux linkage on the stator during motor running; therefore, the flux linkage observation can be omitted. Closed-loop control of torque is achieved by a Bang-Bang controller.

As shown in Figure 4(a), the difference $\Delta T$ between given value $T_e^*$ and actual value $T_e$ is compared with $\varepsilon_m$ and $-\varepsilon_m$ in torque controller. In the case that $\Delta T$ is smaller than $-\varepsilon_m$, the torque controller will output 1, then the non-zero voltage space vector provided by voltage vector selection table is selected, so that the stator flux linkage rotates forward, and flux angle increases. As a result, the actual value $T_e$ increases, and difference $\Delta T$ increases. When $\Delta T$ is larger than $\varepsilon_m$, the torque controller will output 0, and the zero voltage space vector is selected. The stator flux linkage does not rotate; flux angle decreases; the actual value $T_e$ decreases; difference $\Delta T$ increases. The adjustment process is shown in Figure 4(b), and the switcher table is as indicated in Table 1.

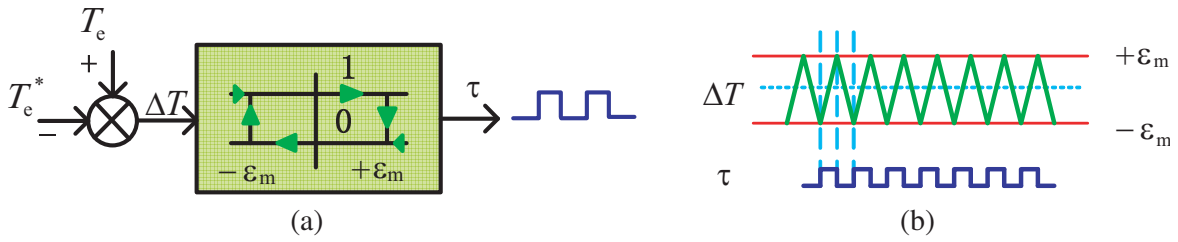


**Figure 4.** Torque adjustment. (a) Bang-Bang controller. (b) Torque adjustment principle.

**Table 1.** Voltage vector selection table.

| $\tau$ | Section | | | | | |
|---|---|---|---|---|---|---|
| | **I** | **II** | **III** | **IV** | **V** | **VI** |
| **1** | $v_5$ | $v_6$ | $v_1$ | $v_2$ | $v_3$ | $v_4$ |
| **0** | $v_0$ | $v_0$ | $v_0$ | $v_0$ | $v_0$ | $v_0$ |

According to the analysis of the mathematical model of the BBLDC motor, decoupling control is not required between the torque winding and suspension force winding when using DTC to control motor.

### 3.2. Analysis of Commutation Torque Ripple in the DTC Scheme

DTC scheme can effectively reduce torque ripple, but it will lose restriction on commutation torque ripple when the motor is running at high speed. Considering the situation that commutation current changes from phase $B$ to $C$, and phase $A$ is the non-commutation phase. During the commutation period:

$$\begin{cases} e_a = -E_m, & e_b = e_c = E_m \\ U_a = U_b = 0, & U_c = U_{bus} \\ i_a + i_b + i_c = 0 \end{cases} \tag{14}$$

where $E_m$ is the peak value of back EMF, and $U_{bus}$ is the bus voltage. Substituting Equation (14) into Equation (1) yields:

$$3Ri_a + 3L\frac{di_a}{dt} - 4E = -U_{bus} \tag{15}$$

Because the PWM cycle is far less than the electrical constant $L/R$, the influence of the $R$ is ignored. So the equation can be expressed as below:

$$\left\{ i_a = i_{a0} + \frac{4E - U_{bus}}{3L}, \quad i_b = i_{b0} + \frac{-2E - U_{bus}}{3L}, \quad i_c = i_{c0} + \frac{2U_{bus} - 2E}{3L} \right. \tag{16}$$

where $i_{a0}$, $i_{b0}$ and $i_{c0}$ are initial current values of phases $A$, $B$ and $C$, $i_{a0} = i_0$, $i_{b0} = i_0$, $i_{c0} = 0$.

Then commutation torque can be figured out from torque expression:

$$T_e = \frac{2E_m i_0}{\omega} + \frac{2E_m}{3L\omega}(U_{bus} - 4E_m) \tag{17}$$

The initial commutation torque is:

$$T_e = \frac{2E_m i_0}{\omega} \tag{18}$$

Therefore, torque ripple during the commutation period is:

$$\Delta T_e = \frac{2E_m}{3L\omega}(U_{bus} - 4E_m) \tag{19}$$

where $E_m = \psi_m \cdot \omega$, $\psi_m$ is rotor flux. Formula (19) can be written as:

$$\Delta T_e = \frac{2\psi_m}{3L}(U_{bus} - 4E_m) \tag{20}$$

Electromagnetic torque is proportional to the non-commutation phase current at constant speed. According to the current Equation (16), the commutation current diagram is shown in Figure 5.

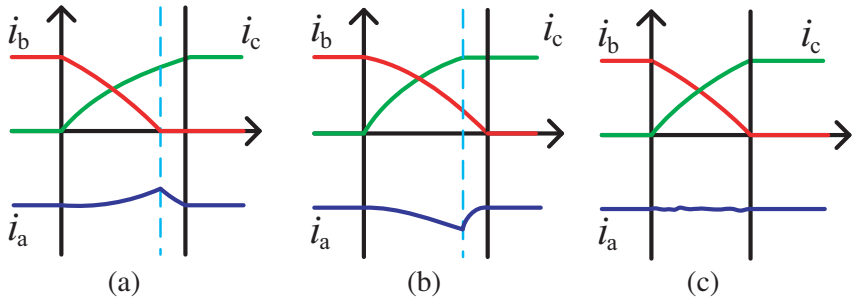


**Figure 5.** Phase current waveform diagram during commutation. (a) $4E > U_{bus}$. (b) $4E < U_{bus}$. (c) $4E = U_{bus}$.

The commutation torque ripple does not occur when the motor rotates at normal speed ($4E_m = U_{bus}$). When motor rotates at low speed ($4E_m < U_{bus}$), the rising speed of current in the upcoming phase is greater than the decreasing speed of current in the outgoing phase during commutation, which causes non-commutation phase current to increase, then torque increases, which can be seen from formula (19). In order to maintain torque stability, according to Section 2.2, DTC will select the zero voltage space vector, then the currents of upcoming phase and non-commutation phase are chopped. Finally, the rising speed of current in the upcoming phase and decreasing speed of current in the outgoing phase are equal, and commutation torque ripple is controlled.

When motor rotates at high speed ($4E_m > U_{bus}$), the rising speed of current in the upcoming phase is less than the decreasing speed of current in the outgoing phase during commutation; non-commutation phase current decreases, then torque decreases. In order to maintain torque stability, the decreasing speed of current in the outgoing phase should be slowed, or the rising speed of current in the upcoming phase should be accelerated. However, the outgoing phase cannot be controlled, and DTC does not accelerate the rising speed of current in the upcoming phase. As a result, DTC will fail to maintain torque stability. Therefore, a new method is needed to reduce the commutation torque ripple.

### 3.3. Improvement of DTC Scheme

#### *3.3.1. Principle of CPC*

From the above analysis, the commutation torque ripple can be reduced by suppressing the non-commutation phase current ripple. CPC takes the non-commutation current as the object of prediction control, and the purpose is keeping the non-commutation current constant by changing the rising speed of current in the upcoming phase and the decreasing speed of current in the outgoing phase.

Taking the motor running in the high speed range for an example, assuming that phase $B$ is the outgoing phase, and its duty cycle is $D_B$ determined by the output of prediction control law. Phase $C$ is the upcoming phase, and its duty cycle is 1. Phase $A$ is the non-commutation phase. Three phase voltage equations are as follows during the commutation:

$$\begin{cases} U_A = Ri_a + L\dfrac{di_a}{dt} + e_a + U_N \\ U_B = Ri_b + L\dfrac{di_b}{dt} + e_b + U_N = U_{bus} \times D_B \\ U_C = Ri_c + L\dfrac{di_c}{dt} + e_c + U_N = U_{bus} \end{cases} \tag{21}$$

Then $U_{BA}$ can be expressed as follows:

$$U_{BA} = -3Ri_a - 3L\frac{di_a}{dt} + 4E - U_{bus} = 3Ri + 3L\frac{di}{dt} + 4E - U_{bus} = U_{bus} \times D_B \tag{22}$$

After discretizing:

$$U_{BA(k)} = 3Ri_{(k)} + \frac{3L}{T}\left[i^*_{(k+1)} - i_{(k)}\right] + 4E_{(k)} - U_{bus} = U_{bus} \times D_B \tag{23}$$

where $T$ is the sampling time, and $i$ is the current amplitude of phase $A$. Formula (23) is the expression of CPC. It means that at the time of $k$, voltage calculated by the formula above is applied between the outgoing phase and non-commutation phase windings, the non-commutation phase current will achieve the desired current value at time $k+1$.

Similarly, when motor is running in the low speed range, we can get the following expression:

$$U_{CA(k)} = 3Ri_{(k)} + \frac{3L}{T}\left[i^*_{(k+1)} - i_{(k)}\right] + 4E_{(k)} = U_{bus} \times D_C \tag{24}$$

Its means that at the time of $k$, voltage calculated by the formula above is applied between the upcoming phase and non-commutation phase windings, and the non-commutation phase current will achieve the desired current value at time $k+1$.

### *3.3.2. Control Strategy Implementation*

In the above theoretical analysis, we get different expressions of CPC in the high speed range and low speed range, but we need a strategy applicable within the full speed range in practical engineering applications.

In order to control the outgoing phase, this paper uses overlapping commutation technology. Outgoing phase is turned off with some delay during the commutation period. Meanwhile, the outgoing phase and non-commutation phase are controlled by the method of synchronous PWM modulation, and upcoming phase is always open. The process of system control is shown in Figure 6.

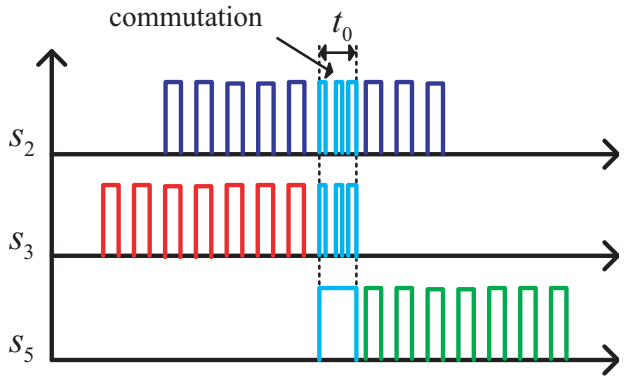


**Figure 6.** The PWM scheme in commutation interval.

When the PWM is at the state of ON, current changes from phase $B$ and phase $C$ to phase $A$, When the PWM is at the state of OFF, $B$ phase current flows through the freewheeling diode located at its lower bridge arm, and $A$ phase current flows through the freewheeling diode located at its upper bridge arm. Three-phase voltage equations are as follows during the commutation:

$$\begin{cases} U_A = (1-D)U_{bus}, & U_B = U_{bus}D, & U_C = U_{bus} \\ U_N = \dfrac{2U_{bus} - E_m}{3}, & \dfrac{di_a}{dt} = \dfrac{di_b}{dt} + \dfrac{di_c}{dt} = 0 \end{cases} \tag{25}$$

From the above equation, the duty cycle $D$ can be figured out:

$$D = \frac{4E_m - 3Ri_a}{3U_{bus}} + \frac{1}{3} \tag{26}$$

After discretizing:

$$D_{(k)} = \frac{4E_m - 3Ri^*_{(k)}}{3U_{bus}} + \frac{1}{3} \tag{27}$$

where $i_a$ is non-commutation phase current. We expect the non-commutation phase current to be constant, so it is treated as a given current.

The duty cycle $D$ cannot be applied in the first control cycle which will affect the control process, so current compensation is required. The schematic diagram of the compensation method is shown in Figure 7, where $|\Delta i_b|$, $|\Delta i_c|$ is the variation of phase current. $K$ is proportional factor.

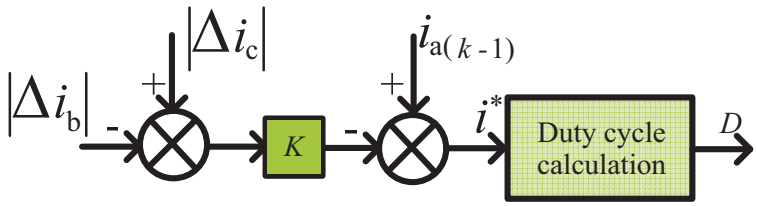


**Figure 7.** Compensation principle diagram.

The block diagram of of BBLDC motor is shown in Figure 8.

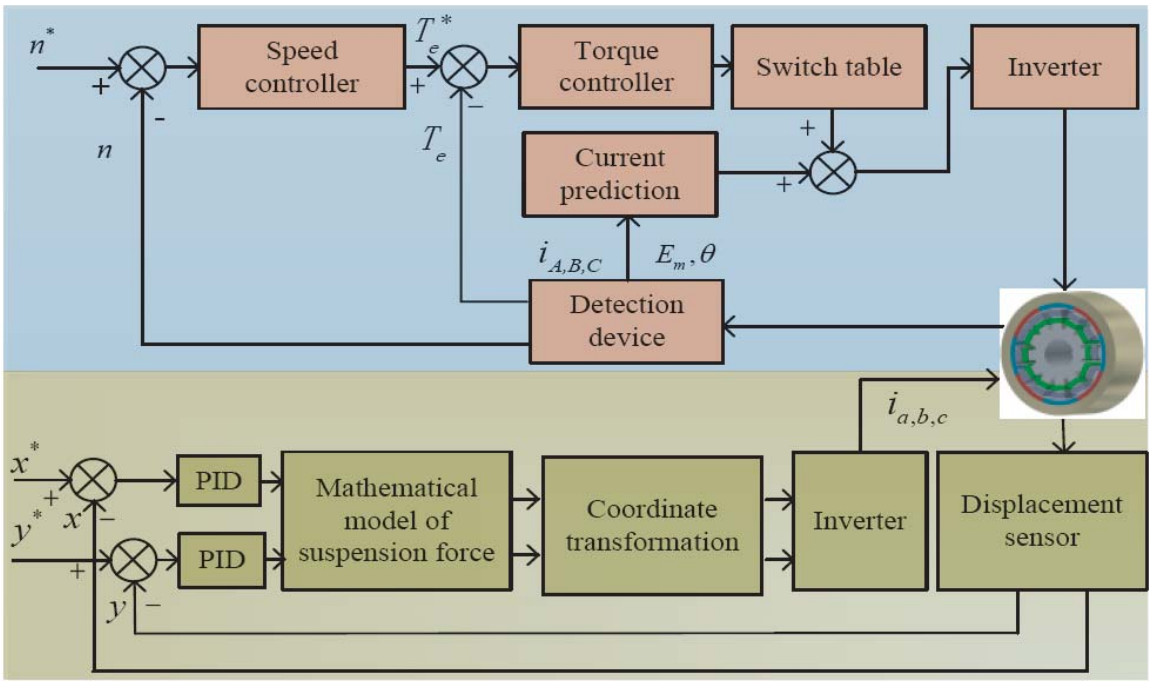


**Figure 8.** System block diagram of BBLDC motor.

Torque control system uses a double closed-loop control strategy for speed and torque. Hall signal changes indicate commutation starts, and then the CPC is adopted. When the current in the outgoing phase is reduced to zero, the commutation is completed, and the DTC is adopted. The given torque is obtained by the speed controller. For the control of the suspension system, the displacement closed loop control strategy is adopted.

## 4. SIMULATION AND RESULTS

According to the motor control schematic diagram and mathematical model, the motor simulation model is established in simulink. The parameters of the motor model are as follows: load torque is $1\,\mathrm{N}\cdot\mathrm{m}$ and applied at 0.05 s; the maximum given torque is $1.2\,\mathrm{N}\cdot\mathrm{m}$; the upper limit of the torque regulator is 0.04; torque winding resistance is $0.35\,\Omega$; torque winding inductance is 4.64 mH; the rotor weight is 1 kg; the moment of inertia is $1.025\times10^{-6}\,\mathrm{kg}\cdot\mathrm{m}^2$.

### 4.1. Simulation and Analysis of Motor Running at High Speed

#### *4.1.1. Simulation Results under Abrupt Load Change*

Figure 9 shows that the motor starts with the maximum given torque. When the load torque changes from 0 to $1\,\mathrm{N}\cdot\mathrm{m}$ at 0.05 s, it can respond quickly within 0.03 s and runs stably. In addition, the torque ripple is effectively controlled within given range, the smaller the given range, the higher the operating frequency of the switch. However, commutation torque ripple is obvious, and the maximum range of fluctuation is $0.14\,\mathrm{N}\cdot\mathrm{m}$. Commutation torque ripple is more than 75 percent of the settings.

Figure 10 shows the results of torque waveform using DTC plus CPC. Comparing Figure 9 with Figure 10, it can be seen that motor still starts with the maximum given torque, but the commutation torque ripple is effectively suppressed when using the proposed approach. Additionally, it also has a

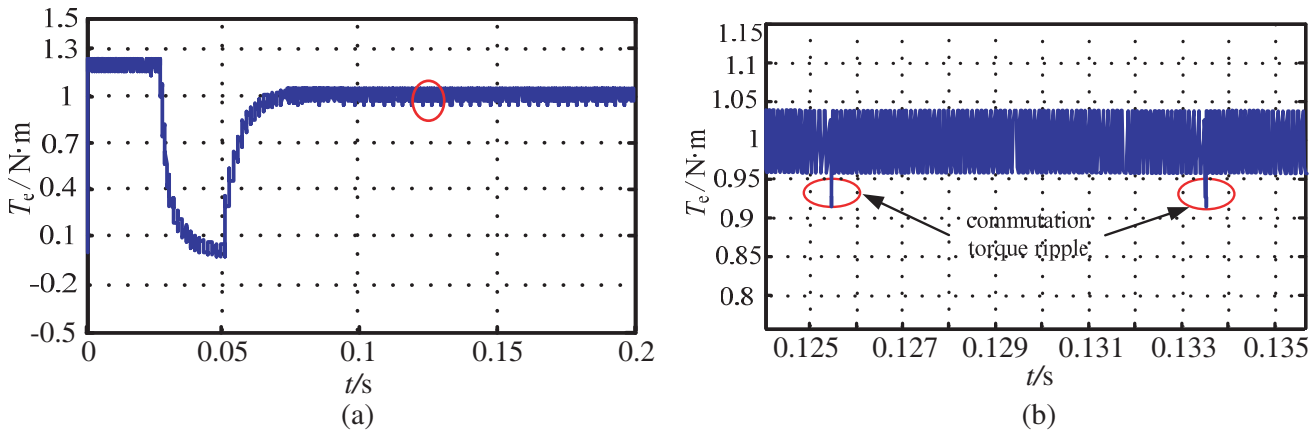


**Figure 9.** Torque waveform using DTC. (a) Torque waveform. (b) Torque waveforms of local enlarged.

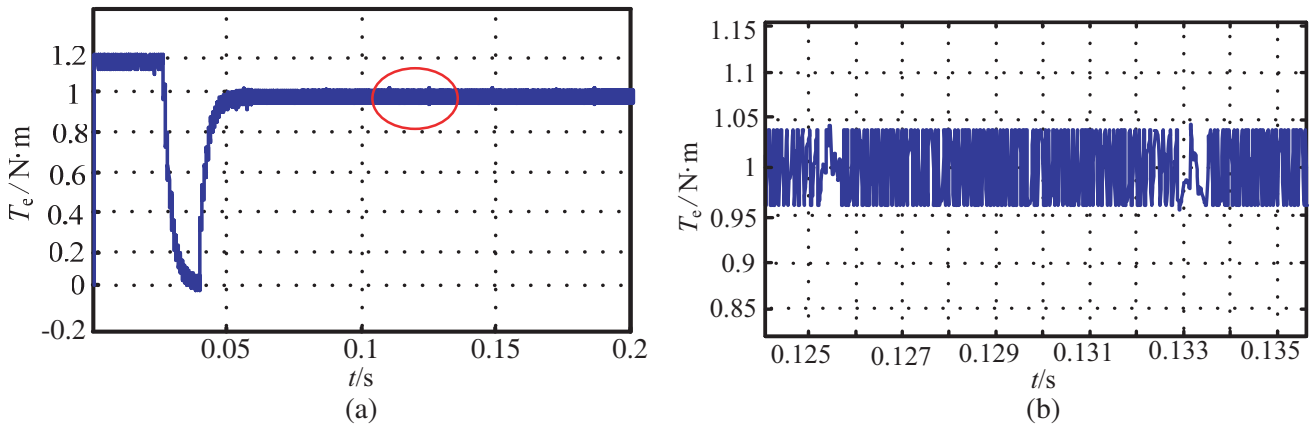


**Figure 10.** Torque waveform using DTC plus CPC. (a) Torque waveform. (b) Torque waveforms of local enlarged.

very fast response speed, and the maximum range of fluctuation is 0.06 N · m.

From Figure 11, the speed is rising fast and has no overshoot. When the load torque changes from 0 to 1 N · m at 0.05 s, the speed varies from 10000 rpm to 9990 rpm correspondingly, and then returns to 10000 rpm within 0.01 s.

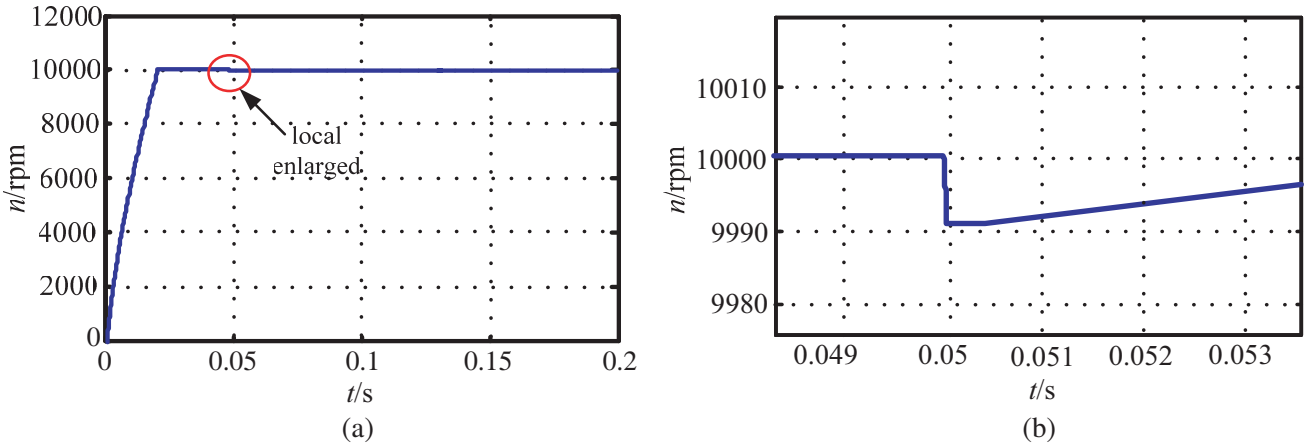


**Figure 11.** Speed waveform using DTC plus CPC. (a) Speed waveform. (b) Speed waveforms of local enlarged.

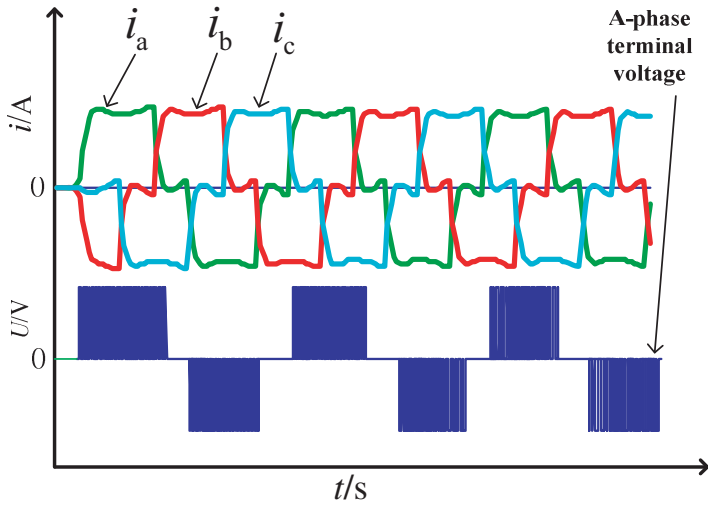


**Figure 12.** Three phase current and A-phase terminal voltage.

According to Figure 12, the change of the current is well controlled, and current waveform is approximately square waveform. A-phase terminal voltage is made up of many small voltage pulses. Figure 13 shows the stator flux trajectory, and it is approximately elliptical. Figure 14 shows that the rotor is stably suspended at 0.03 s, and the maximum jitter value is 0.13 mm.

### *4.1.2. Simulation Results under No Load*

Figure 15 shows the results at high speed under no load. Motor starts with the maximum given torque and runs stably within 0.03 s, and the torque ripple is effectively controlled within a given range 0.08 N·m. The speed is rising fast and has no overshoot. Motor starts with the maximum given torque.

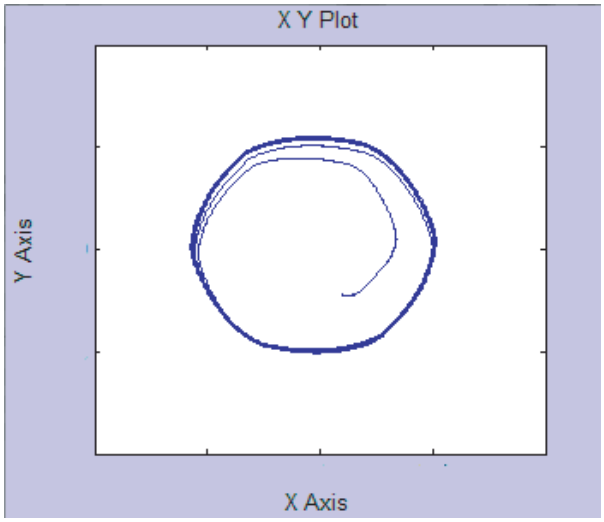


**Figure 13.** Stator flux linkage.

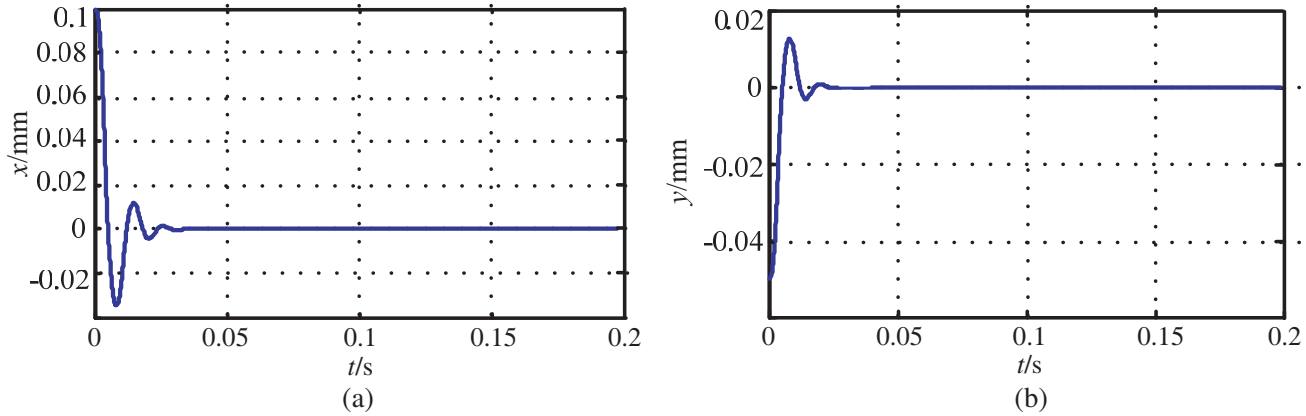


**Figure 14.** Rotor displacement using DTC plus CPC. (a) Displacement along $x$-axis. (b) Displacement along $y$-axis.

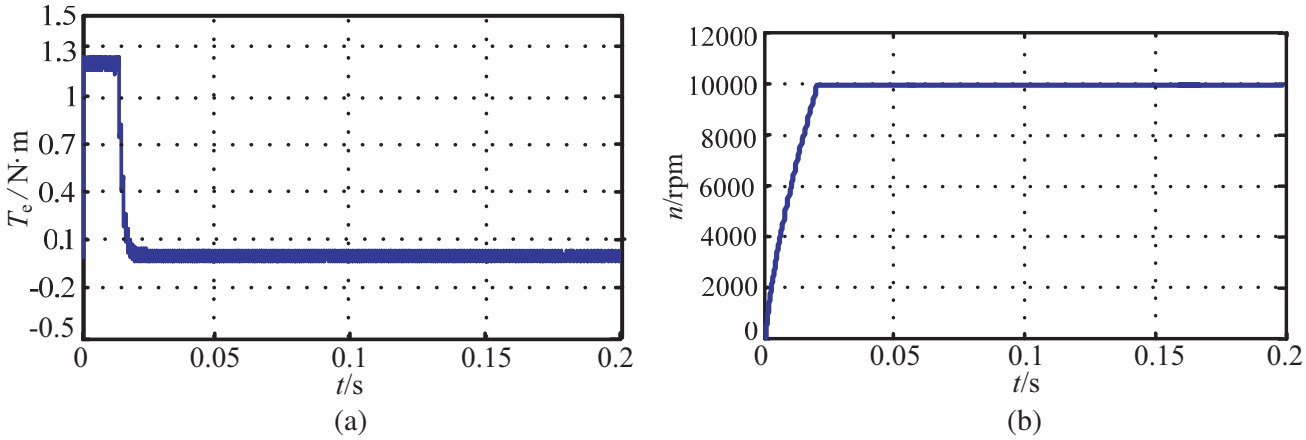


**Figure 15.** Results under no load using DTC plus CPC. (a) Torque waveform under no load. (b) Speed waveform under no load.

### 4.2. Simulation and Analysis of Motor Running at Low Speed

*4.2.1. Simulation Results under Abrupt Load Change*

Figure 16 shows that motor starts with the maximum given torque and torque response within 0.02 s when the torque changes. Furthermore, commutation torque ripple can still be effectively suppressed by the proposed method.

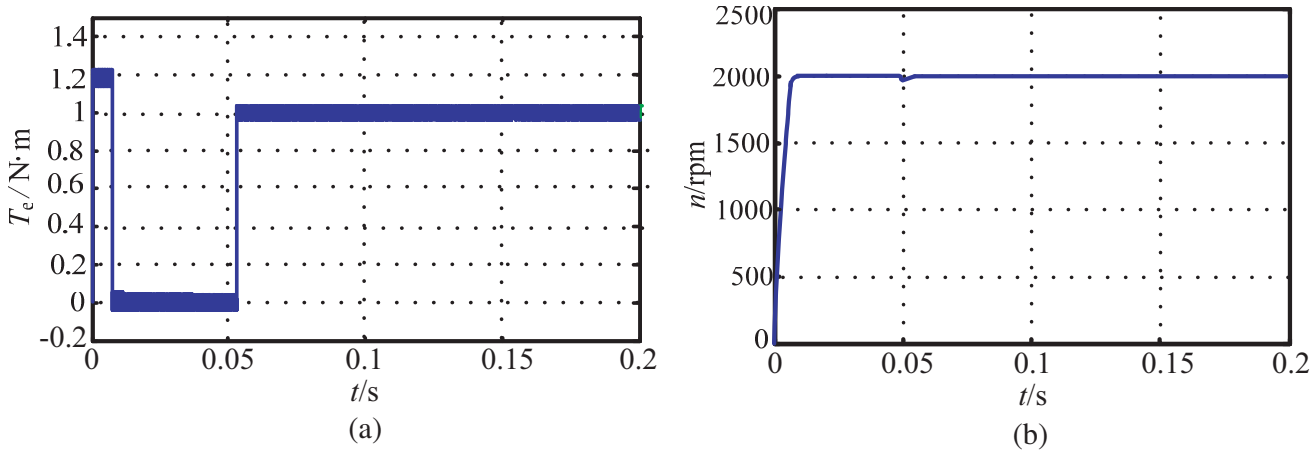


**Figure 16.** Results under abrupt load change using DTC plus CPC. (a) Torque waveform. (b) Speed waveform.

*4.2.2. Simulation Results under No Load*

Figure 17 shows the results at low speed under no load. When running under no load, motor starts with the maximum given torque and runs stably within 0.03 s. The speed is rising fast and has no overshoot.

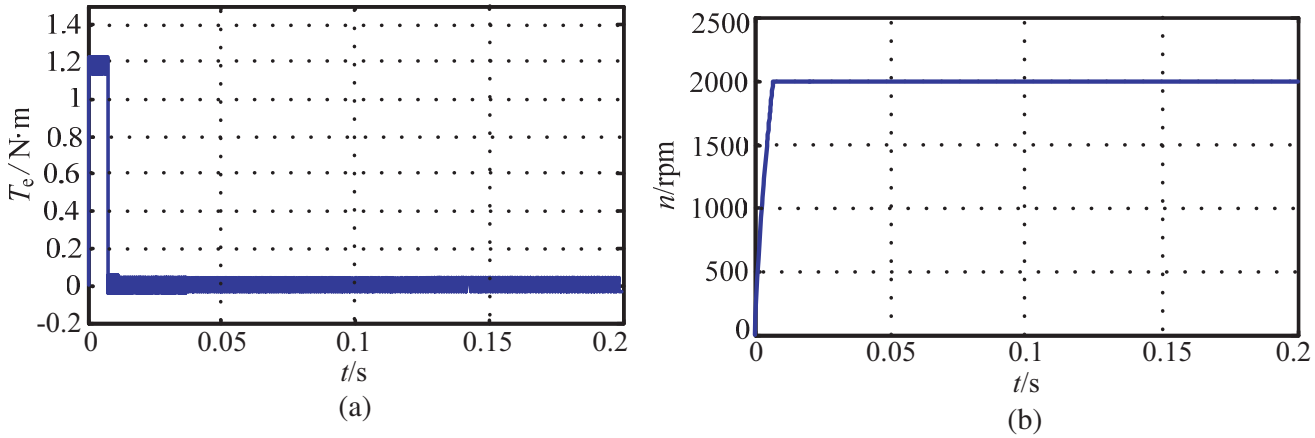


**Figure 17.** Results under no load using DTC plus CPC. (a) Torque waveform. (b) Speed waveform.

### 4.3. Simulation and Analysis of Motor Running at Mutative Speed

Figure 18 shows that the speed changes from 10000 rpm to 2000 rpm at 0.15 s. The speed has no overshoot. Motor starts with the maximum given torque and runs stably within 0.03 s when the load torque is applied. When the speed changes from 10000 rpm to 2000 rpm at 0.15 s, torque decreases from 1 N · m to 0 N · m and then returns to 1 N · m within 0.04 s. In addition, commutation torque ripple can still be effectively suppressed.

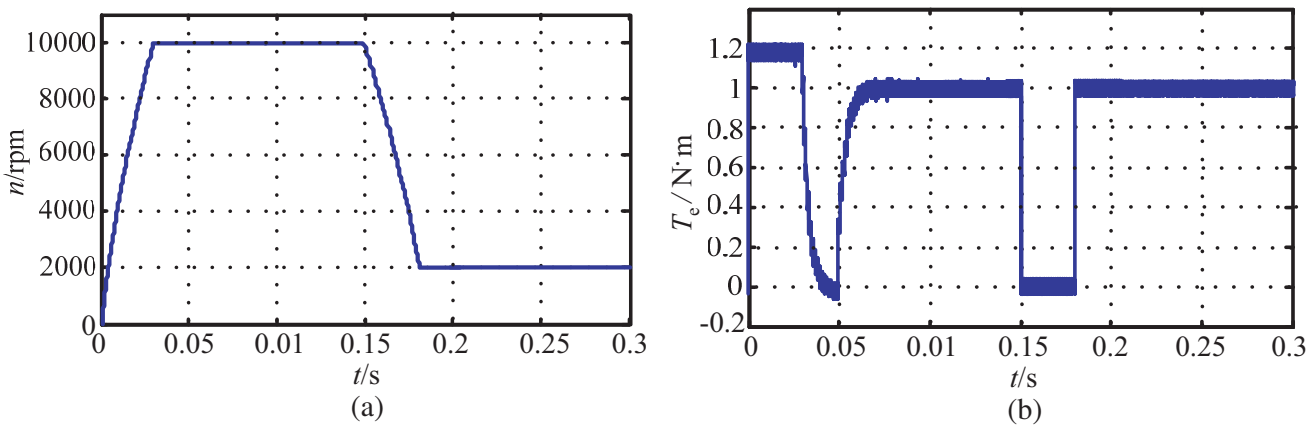


**Figure 18.** Results at mutative speed using DTC plus CPC. (a) Speed waveform. (b) Torque waveform.

## 5. CONCLUSION

This paper introduces the principle of DTC and analyzes the reason of commutation torque ripple when using DTC. In order to simultaneously achieving the suppression of the torque ripple at low speed and high speed in FESS, an approach combines DTC and CPC is proposed. When the motor runs at high speed, it compensates for the non-commutation current drop. When the motor runs at a low speed, the rise of the non-commutation current is weakened and the increase of torque suppressed. In addition, the suspension performance of the rotor is not affected. This method avoids adding extra hardware circuits and topology and has the advantages of fast torque response and good robustness.

## ACKNOWLEDGMENT

This work was sponsored by the National Natural Science Foundation of China (51707082, 51607080), Natural Science Foundation of Jiangsu Province (BK20170546), China Postdoctoral Science Foundation (2017M620192) and the Priority Academic Program Development of Jiangsu Higher Education Institutions.

## REFERENCES

1. Ooshima, M. and C. Takeuchi, "Magnetic suspension performance of a bearingless brushless DC motor for small liquid pumps," *IEEE Transactions on Industry Applications*, Vol. 47, No. 1, 72–78, 2011.
2. Sun, Y., F. Yang, and Y. Yuan, "Control of out-rotor bearingless brushless DC motor," *2017 32nd Youth Academic Annual Conference of Chinese Association of Automation (YAC)*, 624–627, IEEE, 2017.
3. Takahashi, I. and T. Noguchi, "A new quick-response and high-efficiency control strategy of an induction motor," *IEEE Transactions on Industry Applications*, No. 5, 820–827, 1986.
4. Ozturk, S. B. and H. A. Toliyat, "Direct torque and indirect flux control of brushless DC motor," *IEEE/ASME Transactions on Mechatronics*, Vol. 16, No. 2, 351–360, 2011.
5. Wang, W. H. and H. B. Huang, : "Research on commutation fluctuation self-adaptive control suppression strategy for brushless DC motor," *2012 10th World Congress on Intelligent Control and Automation (WCICA)*, 265–269, IEEE, 2012.
6. Kim, D. K., K. W. Lee, and B. I. Kwon, "Commutation torque ripple reduction in a position sensorless brushless DC motor drive," *IEEE Transactions on Power Electronics*, Vol. 21, No. 6, 1762–1768, 2006.

7. Fakham, H., M. Djemai, and K. Busawon, "Design and practical implementation of a back-EMF sliding-mode observer for a brushless DC motor," *IET Electric Power Applications*, Vol. 2, No. 6, 353–361, 2008.
8. Kumar, B. P. and C. M. C. Krishnan, "Comparative study of different control algorithms on brushless DC motors," *2016 Biennial International Conference on Power and Energy Systems: Towards Sustainable Energy (PESTSE)*, 1–5, IEEE, 2016,
9. Liu, Y., Z. Q. Zhu, and D. Howe, "Direct torque control of brushless DC drives with reduced torque ripple," *IEEE Transactions on Industry Applications*, Vol. 41, No. 2, 599–608, 2005.
10. Pan, H., M. Gu, and J. Gu, "A kind of simplified structure direct torque control method for brushless DC motor," *2013 Third International Conference on Instrumentation, Measurement, Computer, Communication and Control (IMCCC)*, 1480–1483, IEEE, 2013.
11. Li, D., J. Yang, and Y. Dou, "Comparison analysis for pure torque loop control of brushless DC motor," *2016 19th International Conference on Electrical Machines and Systems (ICEMS)*, 1–4, IEEE, 2016.
12. Kang, S. J. and S. K. Sul, "Direct torque control of brushless DC motor with no ideal trapezoidal back EMF," *IEEE Transactions on Power Electronics*, Vol. 10, No. 6, 796–802, 1995.
13. Lai, Y. S. and J. H. Chen, "A new approach to direct torque control of induction motor drives for constant inverter switching frequency and torque ripple reduction," *IEEE Transactions on Energy Conversion*, Vol. 16, No. 3, 220–227, 2001.
14. Liu, Y., Z. Q. Zhu, and D. Howe, "Commutation-torque-ripple minimization in direct-torque-controlled PM brushless DC drives," *IEEE Transactions on Industry Applications*, Vol. 43, No. 4, 1012–1021, 2007.
15. Zhang, J., J. Chai, and X. Sun, "Predictive current control for dual three phase induction machine with phase locked loop based electromotive force prediction," *2014 17th International Conference on Electrical Machines and Systems (ICEMS)*, 114–117, IEEE, 2014.
16. Park, J., Y. Kwak, and Y. Jo, "Torque ripple reduction of BLDC motor using predicted current control," *2016 IEEE Conference and Expo Transportation Electrification Asia-Pacific (ITEC Asia-Pacific)*, 407–411, IEEE, 2016.
17. Wei, G., C. Zhen, and Z. Jing, "Modified current prediction control strategy for suppressing commutation torque ripple in brushless DC motor," *Proceedings 2013 International Conference on Mechatronic Sciences, Electric Engineering and Computer (MEC)*, 3770–3774, IEEE, 2013.